A Model for the Derivation of Fuel Budgets in Multistatic SAR Formations

Reuben Katz[a,b], Jalal Matar[a], Eduardo Rodrigues-Silva[a], Marc Rodriguez-Cassola[a], Felix Antreich[b], Gerhard Krieger[a], and Alberto Moreira[a]
[a]German Aerospace Center (DLR), Oberpfaffenhofen, Germany
[b]Aeronautics Institute of Technology (ITA), São José dos Campos, Brazil

Abstract

The use of multistatic SAR concepts offers a clear path for spacecraft simplification while targeting decent to good image quality and characteristics, typically linked to very stringent navigation requirements. In this complex multi-dimensional optimization trade space, the allocation of the fuel budget is of equivalent importance to other critical parameters such as instrument mass or power consumption. This paper focuses on fuel budget optimization under challenging baseline maintenance requirements. The problem is split into two consecutive parts: i) the maintenance of the reference track within a tube of several tens of meters to allow for repeat-pass SAR interferometric applications, and ii) the maintenance of all satellites in the formation within very tight cross-track and along-track baselines to allow for successful multistatic SAR reconstruction techniques. The paper describes the model used for the analysis and estimates of the required fuel in realistic multistatic scenarios.

1 Introduction

The problem statement of the paper is the following: provide fuel consumption estimates relevant for small satellites in formation via a realistic satellite simulator. The analysis will be focused on multistatic SAR systems, which require two complementary orbital control strategies: i) the control of all satellites of the formation within a tube of several tens of meters to allow for repeat-pass interferometric applications and ii) the control of the baselines between the elements of the formation within along-track and cross-track margins of decimeters and meters, respectively. In some of the advantageous cases, the paper shows fuel budgets for a 5-year period in both strategies, which are in the order of 5 to 10% of the spacecraft mass for the latter case and less than 1% of the spacecraft's mass for the former case.

In [1, 2], the authors show results in terms of delta-v considering large platforms (over 1 ton) for one operating altitude and a single orbital tube size. Here, we will conduct an analysis for smaller platforms and verify if fuel is a system driver when considering smaller tubes and different altitudes of operation. Additionally, in [3], the authors consider four different natural formations while achieving control errors one order of magnitude higher than the required in this paper. Here, we analyze forced configurations (*i.e.*, satellites in formation that must be controlled to maintain the desired configuration), as well as analyze the necessary fuel to achieve the required control accuracy.

Table 1 displays the reference values used for the simulations.

Area drag	3.2 m^2
Area Solar Radiation Pressure	7.7 m^2
Mass	400 kg
Altitude	770 km
I_{sp}	230 s

Table 1 Used satellite parameters.

In the following sections, our analysis will commence with an examination of an absolute orbit maintenance strategy and incorporate it into a simulation to determine the required delta-v per year. Subsequently, we will display a formation flying strategy and determine its necessary delta-v for a 5-year period. Finally, a technological survey will be shown, displaying formation flying sensors to assess their impact on the system's overall power and mass.

2 Station Keeping or Flying within an Orbital Tube for the Reference Track

As discussed above, we are first interested in quantifying the implications of keeping an orbital tube for the reference mission to allow for repeat-pass interferometric applications [1, 2] through a sun-synchronous, repeat-ground track near-polar frozen orbit. As sufficiently known, the radius of the orbital tube is proportional to the carrier frequency (inversely) and the available bandwidth (directly) of the system, which in the case of small satellites may be in the order of tens of meters to a few hundred meters.

Station keeping involves the task of maintaining a satellite in a specific orbit relative to Earth within a certain precision. In the scenario under investigation, we are focusing on a follower-leader configuration. Here, a real satellite (follower) is subjected to all the major perturbations, which are Earth's asphericity, atmospheric drag, solar radiation pressure, and gravitational perturbations from the Sun and the Moon. This real satellite is tasked with following a virtual (fictitious) satellite that is influenced solely by Earth's asphericity.
Regarding operation feasibility, there is a relation between the number of impulses and the size of the orbital tube. A smaller tube size implies more impulses for station keeping. Since these impulses are complex and must be ground-based, there is a direct relationship between the number of impulses and the operational costs of the mission [2].

In our model, we will employ a similar strategy used by previous SAR missions, such as TerraSAR-X [1] and Sentinel-1 [2]. The perturbations considered in the analysis are detailed in Table 2.

Earth's Asphericity	EGM-2008 120x120
Atmospheric Drag	Exponential Model CIRA 72
Solar Radiation Pressure	Cannon Ball Model
Third Body Perturbations	Point Mass Model Sun and Moon

Table 2 Perturbations considered in the analysis.

Let us assume a situation like the one sketched in Fig. 1, with both satellites (virtual and real) having the same along-track position at a given instant in time, denoted as t for the virtual satellite and $t + \Delta t$ for the real satellite. Following [1], the error between the two positions can be

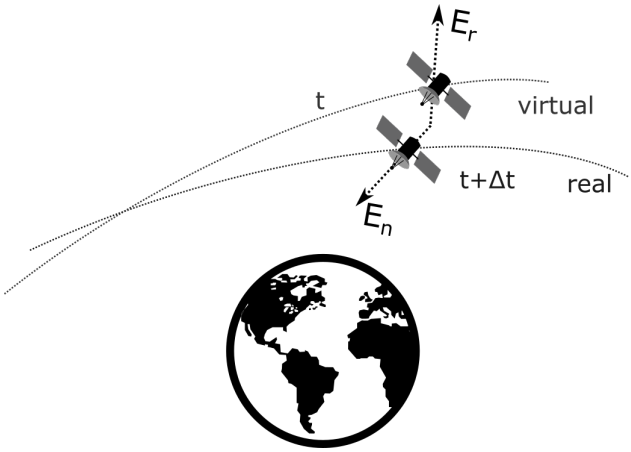

Figure 1 Pseudo-orbital frame of the station keeping strategy.

defined in a pseudo-orbital frame as follows

$$\begin{aligned} E_r &= \Delta a + r_\oplus \Delta e_x \cos(u) + r_\oplus \Delta e_y \sin(u) \ , \\ E_n &= r_\oplus \sin(i) \left[\Delta\lambda \cos(u) + \Delta i \sin(u)\right] \ , \\ E_i &= r_\oplus \Delta i \ , \end{aligned} \tag{1}$$

where E_r describes the radial error and E_i the inclination error. In addition, a third axis denominated E_n - which describes the normal error at all latitudes - is added. In the equations above, $r_\oplus$ is the radial distance between Earth's center and the virtual satellite, Δe_x and Δe_y describe the relative eccentricity vector, $\Delta\lambda$ is the difference in longitude of both satellites, a is the semi-major axis and $u = \omega + f$ the argument of latitude, which is the sum of the argument of perigee and true anomaly respectively. We will also introduce the normal error at the ascending node E_{n0}. In the following subsections, we will describe in-plane corrections, represented by the E_n and E_r components, as well as out-of-plane corrections, represented by the E_i component.

2.1 In-plane Corrections

As previously explained, two values are associated with the in-plane pseudo orbital frame: E_n and E_r. Over time, E_{n0} follows a parabolic trajectory [4], as illustrated in (orange) Fig. 2. In this figure, the vertical axis represents the

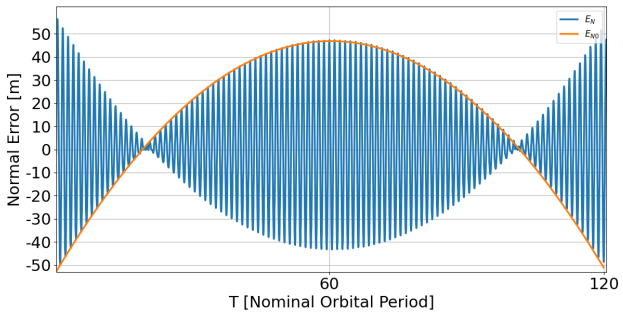

Figure 2 Variation of E_n (blue) and E_{n0} (orange) over time. Here, a thrust would be applied in the semi-major axis as soon as E_{n0} extrapolates the value of the tube (-50 m).

error in meters, while the horizontal axis represents time in nominal orbital periods. These results are based on an altitude of 770 km and a tube size of 50 meters.
The crescent part of this parabolic trajectory occurs when $a_{\text{real}} > a_{\text{virtual}}$, meaning that the real satellite is slower than the virtual satellite, resulting in a temporal separation in longitude. Conversely, the decreasing part of the parabola occurs when $a_{\text{real}} < a_{\text{virtual}}$. Taking this into account, the semi-major axis is adjusted during tube extrapolation. The correction in the semi-major axis is made in a way that the maximum value of the parabola equals the tube size. The corresponding delta-v for this correction can be calculated from the following set of equations

$$\begin{aligned} \Delta a &= \frac{2}{n}\Delta v_T \ , \\ \Delta e_y &= -\gamma \cos(u)\Delta v_N + 2\gamma \sin(u)\Delta v_T \ , \\ \Delta e_x &= -\gamma \sin(u)\Delta v_N + 2\gamma \cos(u)\Delta v_T \ , \\ \Delta i &= \gamma \cos(u)\Delta v_I \ , \end{aligned} \tag{2}$$

where Δv_T represents thrust in the along-track direction, Δv_N represents thrust in the radial direction, Δv_I represents thrust in the direction that completes the Local-Vertical-Local-Horizontal (LVLH) frame, γ represents the inverse of the absolute velocity of the spacecraft and

n the mean motion. When thrust is applied to adjust the semi-major axis, it is done in a manner that positions the argument of latitude in such a way that the relative eccentricity vector is pointing in the opposite direction. This relative position in the argument of latitude can be derived from Eqs. (2).

At altitudes over 550 km, drag is not the primary non-gravitational disturbance. As such, since fewer semi-major axis corrections are required, the eccentricity is directly controlled by applying two thrusts in opposite directions. In this case, it is important to emphasize that since the mass of the satellites under consideration should be smaller than that of already existing missions, solar radiation pressure plays a more significant role in impacting the eccentricity and, as such, the radial error.

2.2 Out-of-plane Corrections

The correction strategy for the out-of-plane error, denoted as E_i, is governed by the last equation in (1). The primary perturbations influencing the deviation in inclination stem from the gravitational effects of the sun and the moon. The adjustment for Δi is orchestrated to maximize the time between consecutive correction maneuvers. Fig. 3 shows the progression of E_i and its correction as a function of the time in orbital periods. It is important to note that the difference in the ascending node $\Delta\Omega$ is not actively controlled in this context. This decision is based on the fact that minor errors in this Keplerian element would not significantly alter the satellite's local time of the ascending node, making it unnecessary to spend additional fuel to control it.

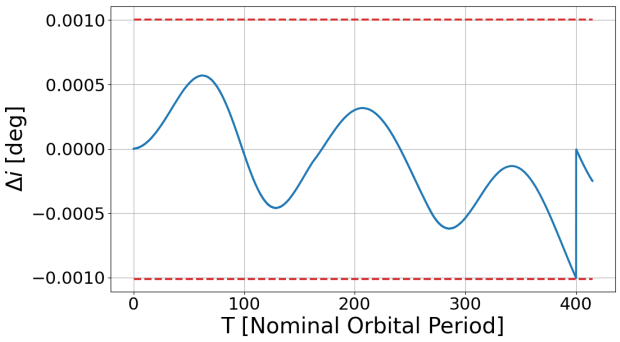

Figure 3 Evolution of inclination error E_i over time. A correction is done around the four hundredth orbital period, when the tube is about to be extrapolated, in such a manner that the overall number of thrusts is minimized.

2.3 Fuel Estimates for Orbital Tube Maintenance

We have considered two tube sizes (radius): 50 meters and 100 meters, *i.e.*, $E_I < \{50, 100\}\ m$, $E_N < \{50, 100\}\ m$ and $E_R < \{50, 100\}\ m$. The results in terms of fuel are displayed in Table 3. These results have been obtained by simulating the orbit maintenance control strategy described in the sections above for 500 orbital periods, then extrapolated for one year. Two results are apparent in

Tube radius [m]	100	50
Total Mass [%/year]	0.27	0.29
Delta-v [m/s/year]	6.13	6.73
Number of impulses out-of-plane [1/year]	52	52
Number of impulses in-plane [1/year]	115	220

Table 3 Results of station keeping for tubes of 100 and 50 m.

Table 3: smaller tubes use more fuel and more impulses, resulting in an increase in mass that can be considered insignificant. As expected, the control of the orbits within tube sizes typically used for interferometry does not seem to drive the design of the spacecraft.

Finally, Fig. 4 shows the impact of the altitude on the fuel budget for orbital tube maintenance. As expected, the increase in altitude decreases drag exponentially. Thus, higher orbits use less fuel for corrections. The small increase of fuel at around 800 km can be expressed by the fact that there is an increase in gravitational perturbations prevenient from third bodies as well as solar radiation pressure.

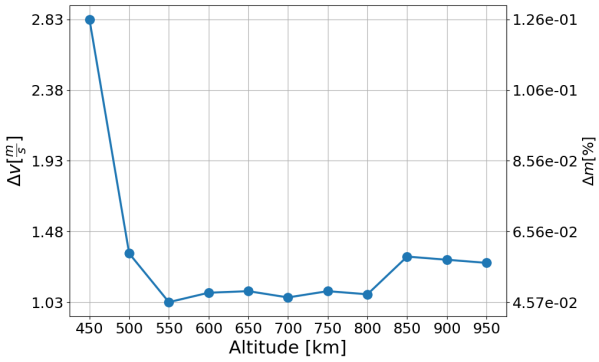

Figure 4 Delta-v per year per altitude for a 200-meter tube.

3 Formation Flying or Keeping an Advantageous Multistatic SAR Formation

As mentioned, the problem of flying advantageous formations for multistatic SAR signal reconstruction typically results in controlling the spacecraft's relative along-track and cross-track positions with accuracies similar to the dimensions of the SAR antennas. In the cases under consideration, the required accuracy in along-track and cross-track are in the order of decimeters and meters, respectively.

The relative motion of free-moving satellites in near-circular Keplerian orbits can be characterized by the Hill-Clohessy-Wiltshire (HCW) equations [5]. These equations describe the movement of a deputy satellite relative to a

chief satellite in the local-vertical-local-horizontal frame. The HCW equations can be complemented to include deviations from the Keplerian model by adding a control vector and orbital perturbations via

$$\begin{aligned} \ddot{x} &= 3n^2x + \dot{y} + \psi_x + u_x \\ \ddot{y} &= -2n\dot{x} + \psi_y + u_y \\ \ddot{z} &= -n^2z + \psi_z + u_z \ , \end{aligned} \tag{3}$$

where x describes the baseline in the radial axis, y in the along-track axis and z completes the reference frame. In addition, $\mathbf{u} = (u_x, u_y, u_z)$ describes the control vector onboard the deputy satellite and $\psi = (\psi_x, \psi_y, \psi_z)$ describes the relative perturbation vector.

The flowchart outlined in Fig. 5 illustrates the entire simulation developed in the scope of this work. Each step in

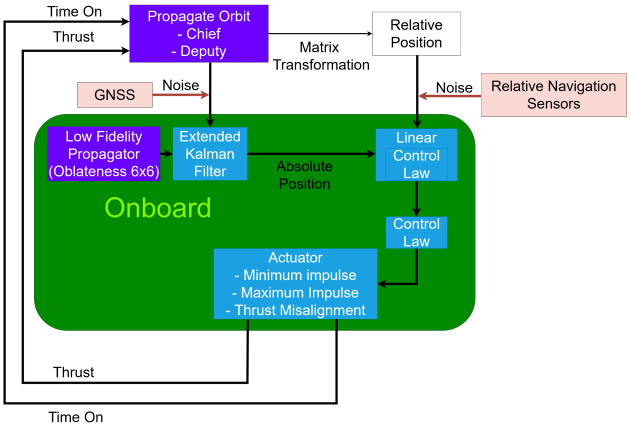

Figure 5 Formation Control Simulation Diagram

blue of the diagram will be explained in detail. In the diagram of Fig. 5, the purple indicates propagation blocks, and the red indicates noise blocks. In this paper, we will consider five deputy satellites. Three configurations were chosen for these spacecraft: a constant along-track baseline formation, a constant cross-track baseline, and a low orbit duty cycle formation in the cross-track direction, which is detailed in [6]. In this section, we will commence by formulating the formation flying problem as a linear matricial equation for a control law. Subsequently, fuel consumption for different formations will be displayed and compared.

3.1 Control Law

Assuming Keplerian motion, (3) can be written in a discrete format with the linear matricial format as follows

$$\mathbf{x}[k+1] = \mathbf{A} \cdot \mathbf{x}[k] + \mathbf{B} \cdot \mathbf{u}[k] \ , \tag{4}$$

where $\mathbf{x}[k] = (x, y, z, \dot{x}, \dot{y}, \dot{z})$ is the state vector. With (4), the discrete format of the LQR can be utilized. This controller is an optimal control technique for linear systems. It minimizes a cost function J defined as a weighted sum of the state variables and the control inputs. The associated cost function can be described via

$$J = \sum_{k=1}^{N-1} \mathbf{x}[k]^T \cdot \mathbf{Q} \cdot \mathbf{x}[k] + \mathbf{u}[k]^T \cdot \mathbf{R} \cdot \mathbf{u}[k] \ , \tag{5}$$

where k represents a time discretization, and the $\mathbf{Q}$ and $\mathbf{R}$ matrix are adjustable weight matrices, which were chosen to be

$$\mathbf{Q} = \begin{bmatrix} n & 0 & 0 & 0 & 0 & 0 \\ 0 & n & 0 & 0 & 0 & 0 \\ 0 & 0 & n & 0 & 0 & 0 \\ 0 & 0 & 0 & 1 & 0 & 0 \\ 0 & 0 & 0 & 0 & 1 & 0 \\ 0 & 0 & 0 & 0 & 0 & 1 \end{bmatrix} , \tag{6}$$

$$\mathbf{R} = \begin{bmatrix} 1/n^2 & 0 & 0 \\ 0 & 1/n^2 & 0 \\ 0 & 0 & 1/n^2 \end{bmatrix} . \tag{7}$$

3.2 Simulation of Error Sources

Two kinds of errors have been incorporated into the simulation: navigation and thrusting errors. We model the navigation error as white Gaussian noise, with a standard deviation of 1 m and 0.1 m/s for absolute positioning and velocity and 10 cm and 0.1 cm/s for relative positioning and velocity, which are directly added to the absolute and relative position and later filtered with an extended Kalman filter. The navigation errors reflect typical accuracies of existing formation flying sensors, which are detailed in section 4.

The thrusting errors are aimed at simulating errors in the impulses. Here, we consider a 1-N thruster with a minimum impulse bit of 0.175 Ns. Fig. 6 shows the three variables: γ, δ and δF related to thrusting misalignment. The γ and δ angles describe a 2-D misalignment in the impulse and δF the modulus of the error. These three variables are

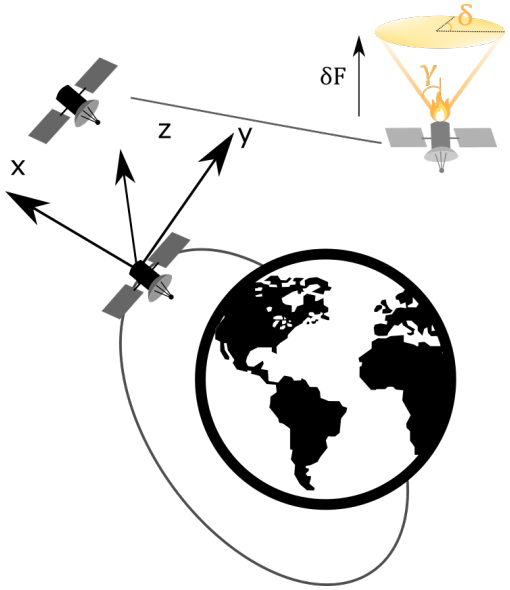

Figure 6 This figure illustrates the reference frame in (3) and the three thrusting misalignment variables.

represented as random processes. The parameters for this simulated distribution are as follows: γ is uniformly distributed from 0° to 360°, δ is a Gaussian variable with a 3σ confidence of 1°, and δF is also a Gaussian with a 3σ confidence of 10% of the applied thrust.

3.3 Fuel Consumption for Formation Control

Fig. 7, 8, and 9 display the fuel consumption for different formations, considering a simulation period of one day.

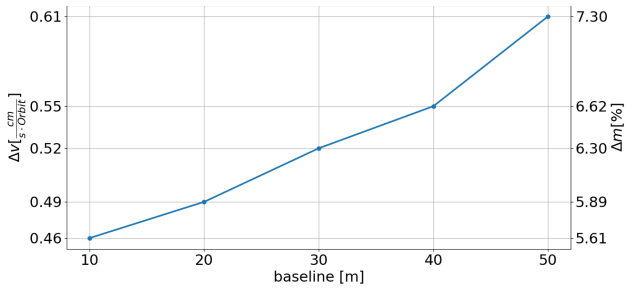

Figure 7 Increase of required delta-v per orbit and the corresponding fuel mass change for maintaining an along-track formation as a function of baseline.

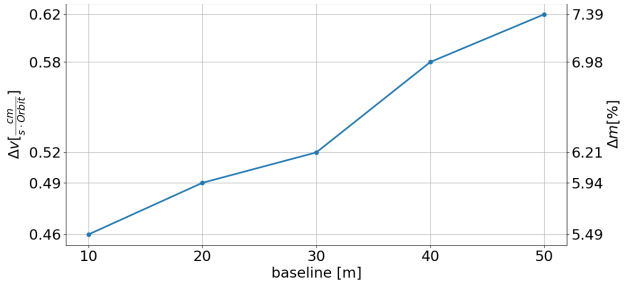

Figure 8 Increase of required delta-v per orbit and the corresponding fuel mass change for maintaining a cross-track formation with low orbit duty cycle as a function of baseline.

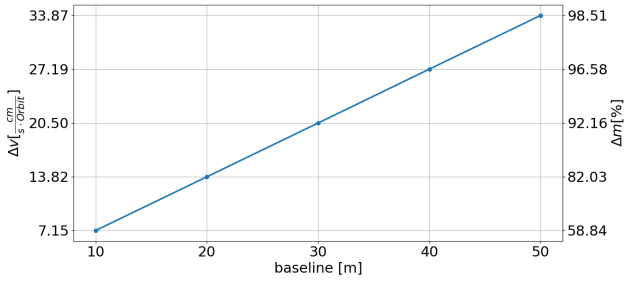

Figure 9 Increase of required delta-v per orbit and the corresponding fuel mass change for maintaining a cross-track formation with high orbit duty cycle as a function of baseline.

In all cases, the ordinates represent the delta-v per orbit in cm/s. The adjacent vertical axis shows the corresponding fuel in terms of percent of wet mass for five years of operation and a 100% SAR instrument duty cycle for the described propulsion system. In the first two cases, which correspond to along-track formations or cross-track formations of opportunity (i.e., possibly with low orbit duty cycles), the simulations do not show the fuel as a system driver. In the last case, corresponding to a cross-track formation that must be maintained persistently - hence allowing for high orbit duty cycles from that perspective - the fuel takes as much mass as the whole spacecraft within five years. This extrapolation of the mass budget aligns with what can be seen in [7]. Thus, despite its advantageous duty cycle, this formation is unfeasible due to its high fuel consumption.

In terms of control margins, the mean control error increases with the increase of the baseline; as such, we will analyze the worst case, which corresponds to the 50-meter baseline. The formation in Fig. 7 has relative positioning accuracy in the along-track direction of around 30 cm and cross-track direction of around 15 cm. Furthermore, the formation in Fig. 8 has a mean error in the along-track direction of around 50 cm and error in the cross-track direction of around 15 cm – as such, both configurations attend the required accuracy.

4 Technological Survey

This section offers a summary of the relative navigation sensors applicable to the systems under consideration, drawing from elements utilized in previously launched formation flying missions. The most pertinent systems for short-baseline formations encompass vision-based sensors (VBS), LIDAR systems, and differential GNSS (DGNSS). These sensors will be evaluated in terms of real-time accuracy, mass, and power consumption. A recommendation for the considered case will be provided based on a Pugh decision matrix.

LIDAR systems typically have accuracies in the order of mm in real-time but must be considered in the spacecraft power and weight budget. Table 4 shows that, from three formation flying missions with a LIDAR system, the average mass is 20 kg, and the average power is 36 W. Since millimeter-range precision is unnecessary for this real-time application, this system does not seem attractive for the scenario under consideration due to its high power consumption.

VBS achieves centimeter accuracy with low power consumption and mass, with their main energy consumption prevenient from light-emitter diodes for feature extraction. Table 4 displays VBS and LEDs used in previous missions. Additionally, cameras have the advantage of obtaining relative pose between the satellites.

Finally, DGNSS can achieve relative accuracy at the decimeter level and use even less power and mass than a vision-based sensor, but it requires constant communication links between the satellites and may suffer from occasional unavailability and multipath issues. Table 4 also shows GNSS receivers without flight heritage.
To compare these sensors, a Pugh decision matrix is formulated in terms of accuracy, power, and mass. Table 5 shows this matrix, indicating that the GNSS sensor and VBS are the most appropriate sensors for the analyzed formations.

Sensor	Mission	Weight [kg]	Power [W]
LIDAR	Gemini [8]	30	40
	Grace [9]	20	35
	DART/Orbit Express [10]	10	35
average =		20	36
VBS+LED	AAReST [11]	4	< 3.5
	Proba 3 (7 LEDs) [12]	4.5	12.3
	PRISMA (4 LEDs) [12]	< 1	< 9
average =		3.2	8.3
DGNSS	Pheonix (PRISMA) [13]	20 g	0.9
	OEM-615 (CanX Legacy) [14]	24 g	1.1
	GNS-701 [15]	160 g	2.2
average =		68 g	1.4

Table 4 Formation Flying Sensors Powers and Mass.

	GNSS	VBS	LIDAR
Accuracy	2	4	5
Power	5	3	1
Mass	5	4	1
Sum	12	11	7
Rank	1	2	3

Table 5 Comparison of GNSS, VBS, and LIDAR based on Accuracy, Power, and Mass.

5 Conclusion

In summary, this paper presented a practical simulation to estimate fuel consumption for a multistatic SAR mission. Concerning orbital tube maintenance, our conclusions underscore that fuel is not a system driver in terms of mass, using around 0.6 % percent per year for a 50-meter orbital tube. Additionally, fuel consumption tends to decrease with increasing altitude, driven by the exponential decay of drag. An exception occurs around 800 km due to third-body perturbations and solar radiation pressure, causing a slight uptick.

Regarding satellite formation flying, our analysis reveals that a five-year operation utilizes only 5-10% of the spacecraft mass for both along-track and low orbit duty cycle formations while achieving a relative baseline control accuracy in the order of decimeters in the along-track direction and meters in the cross-track axis.

Lastly, in our technological survey, we found that for small baselines, DGNSS techniques and VBS emerge as the most suitable options, producing a relative positioning accuracy of 10 cm and velocity accuracy of 0.1 mm/s.

6 Acknowledgment

This study was financed in part by the Coordenação de Aperfeiçoamento de Pessoal de Nível Superior – Brazil (CAPES) – Finance Code 001.

7 Literature

[1] R. Kahle and S. D'Amico, "The TerraSAR-X Precise Orbit Control - Concept and Flight Results," in *International Symposium on Space Flight Dynamics (ISSFD)*, 2014.

[2] M. M. Serrano, I. Shurmer, and X. Marc, "Sentinel-1: Operational approach to the orbit control strategy," *Proceedings of the 23d ISSFD*, 2012.

[3] P. Bodin *et al.*, "Prisma Formation Flying Demonstrator: Overview and Conclusions from the Nominal Mission," *Advances in the Astronautical Sciences*, vol. 144, 02 2012.

[4] W. McClain and D. Vallado, *Fundamentals of Astrodynamics and Applications*. Springer Science & Business Media, 2001, vol. 12.

[5] W. H. Clohessy and R. S. Wiltshire, "Terminal Guidance System for Satellite Rendezvous," *Journal of the Aerospace Sciences*, vol. 27, no. 9, pp. 653–658, 1960.

[6] G. Krieger *et al.*, "TanDEM-X: A Radar Interferometer with Two Formation Flying Satellites," *Acta Astronautica*, vol. 89, pp. 83–98, 08 2013.

[7] M. Martín-Neira *et al.*, "TriHex: Combining Formation Flying, General Circular Orbits, and Alias-Free Imaging, for High-Resolution L-B and Aperture Synthesis," *IEEE Transactions on Geoscience and Remote Sensing*, vol. 61, pp. 1–17, 2023.

[8] E. K. A. Gill, M. Steckling, and P. Butz, "Gemini: A Milestone toward Autonomous Formation Flying," 2001. [Online]. Available: https://api.semanticscholar.org/CorpusID:55443930

[9] K. Abich *et al.*, "In-Orbit Performance of the GRACE Follow-on Laser Ranging Interferometer," *Phys. Rev. Lett.*, vol. 123, p. 031101, Jul 2019.

[10] R. Howard and T. Bryan, "The Next Generation Advanced Video Guidance Sensor: Flight Heritage and Current Development," *AIP Conference Proceedings*, vol. 1103, pp. 615–621, 03 2009.

[11] C. B. Craig Underwood. AAReST Spacecraft Update: Spacecraft Bus, Propulsion, ADCS, SSTL-50 CoreSat, RDV/Docking, OBDH and Comms. [Online]. Available: .http://www.its.caltech.edu/~sslab/AAReST_Docs/AAReST_Payload_CDR_Surrey_Update.pdf

[12] J. Jørgensen, T. Denver, and P. Jørgensen, "Using an autonomous star tracker as formation flying sensor," *Proceedings of the 4S Symposium: Small Satellites, Systems and Services (ESA SP-571)*, 11 2004.

[13] M. Markgraf. Phoenix: Spaceborne GPS Receiver. (accessed:18.01.2024). [Online]. Available: https://www.dlr.de/rb/en/Portaldata/38/Resources/dokumente/GSOC_dokumente/RB-RFT/Phoenix_DataSheet_v11.pdf

[14] Novatel. Receivers OEM615. (accessed:18.01.2024). [Online]. Available: https://hexagondownloads.blob.core.windows.net/public/Novatel/assets/Documents/Papers/OEM615/OEM615.pdf

[15] GNS Electronics. GNS 701. (accessed:18.01.2024). [Online]. Available: https://www.gns-electronics.de/wp-content/uploads/2019/10/GNS701_datasheet_V014.pdf